*Manuscript: Thin Solid Films, in press, 2019: https://doi.org/10.1016/j.tsf.2019.05.003

First principles investigation into the phase stability and enhanced hardness of TiN-ScN and TiN-YN alloys

V. Adhikari[1,†], N. J. Szymanski[1,†], I. Khatri[1], D. Gall[2], S. V. Khare[1*]

[1]*Department of Physics and Astronomy, The University of Toledo, 2801 West Bancroft Street, Toledo, OH 43606, USA*
[2]*Department of Materials Science and Engineering, Rensselaer Polytechnic Institute, 110 8th Street, Troy, NY 12180, USA*

* Corresponding author: sanjay.khare@utoledo.edu
† Authors V. Adhikari and N. J. Szymanski have contributed equally.

Abstract

We study the phase stability, mechanical properties, and electronic structure of two quasi-binary ceramic systems, $Ti_{1-x}Sc_xN$ and $Ti_{1-x}Y_xN$ ($0 \leq x \leq 1$), using first principles methods based on density functional theory, cluster expansion formalism, and Monte Carlo techniques. Owing to the similarity in ionic radii and electronegativities of their respective transition metals, strong exothermic mixing of TiN and ScN is predicted, with four ordered intermetallic phases lying on the convex hull: $TiScN_2$, $TiSc_8N_9$, $TiSc_9N_{10}$, and $Ti_3Sc_2N_5$. These structures form layered rocksalt-type configurations to minimize strain energy while maximizing occupation of bonding states. The fully-detailed phase diagram including these predicted ground states and known end members is constructed, revealing an upper consolute temperature of 660 K. In contrast to $Ti_{1-x}Sc_xN$, the mismatched properties of TiN and YN lead to large structural distortions and positive strain energies. As a result, endothermic mixing with significant upward bowing in the formation energy is observed at intermediate concentrations. The phase diagram of $Ti_{1-x}Y_xN$ shows that miscibility may only be achieved at either low/high concentrations or at temperatures above 7225 K. TiN, ScN, and YN are found to display hardness values of 24.2, 25.1, and 20.6 GPa respectively, in good agreement with experimental data. The intermetallic phase $Ti_3Sc_2N_5$ is predicted to exhibit an exceptionally high hardness of 27.3 Gpa. From analysis of projected electronic density of states and Crystal Orbital Hamiltonian Populations, we attribute enhanced hardness to strong *d-p* hybridization, being related to $3d$ e_g occupation, and decreased tendency towards shearing, being related to minimal $3d$ t_{2g} occupation. These features extend to the case of random solutions, which we model using special quasirandom structures, showing a maximum hardness at a valence electron concentration of 8.4. Based on these findings, we suggest $Ti_{1-x}Sc_xN$ alloys for implementation in hard coating applications.

1. Introduction

During past couple of decades, transition metal (M) nitrides (TMNs) have drawn significant attention as coating materials due to their high hardness, as well as their resistance to wear and oxidation [1-12]. Many TMNs of the cubic binary form have been explored in the quest for hard coating materials [13-21]. Of these, TiN remains the most widely used compound for modern applications due to its high hardness, robust thermal stability, and low cost of synthesis [22-24, 96, 97]. However, recent works have shown that improved properties may be achieved by alloying TiN with various other transition metals, such as Zr, Hf, V, Nb, Ta, Mo, W [25-35]. Generally, substitution of Ti with these elements, which causes an increase in the valence electron concentration (VEC), leads to enhanced ductility and toughness, coupled with decreased hardness. In contrast, Jhi and Ihm showed that hardness can be increased by decreasing the VEC through replacement of nitrogen with carbon in the TiC_xN_{1-x} system [3, 4]. Further work by Holleck indicated that the hardness of carbonitrides is maximized at a VEC of 8.4 electrons per formula unit [7]. These findings suggest a pathway to enhanced hardness in alloys through changes in bonding behavior, which may also affect microstructural features, which may be influenced by VEC.

Recent investigation into TiN-AlN alloys, synthesized with epitaxial ScN inclusion, have shown enhanced hardness with respect to the end members; however, the application of this system is limited due to its low maximum operating temperature and phase decomposition [36]. Despite their limitations in terms of stability, the properties of $Ti_{1-x}Al_xN$ support the theory that mechanical properties of TMN alloys may be finely tuned through controlled electron valency. $Ti_{1-x}Sc_xN$ has also been studied, showing thermodynamic stability throughout a much wider range of temperatures and concentrations than $Ti_{1-x}Al_xN$, though the electronic and mechanical properties remain unexplored [37, 38]. Considering the similarity in VEC between $Ti_{1-x}Sc_xN$ and $Ti_{1-x}Al_xN$, as well as previous findings regarding the carbonitrides, increased hardness is likely in the TiN-ScN system. If this prediction is confirmed, these alloys would be highly-suitable candidates for hard coating applications.

In this work, we aim to utilize the concept of alloy hardening through controlled VEC to engineer next-generation hard coating systems in the form of $Ti_{1-x}Sc_xN$ and $Ti_{1-x}Y_xN$ alloys for $0 \leq x \leq 1$. We employ state-of-the-art computational modeling techniques based on DFT, cluster expansion techniques, and Monte Carlo formalisms to study the phase stability, electronic structure, and mechanical properties of these materials. In doing so, we identify several novel intermetallic phases exhibiting enhanced hardness with respect to the end members. Additionally, these properties are clearly explained through analysis of projected densities of states (PDOS) and Crystal Orbital Hamiltonian Populations (COHP), each of which elucidating the interplay between e_g-p hybridization and t_{2g} occupation. Our analysis is also extended to the high-temperature case of cation-disordered compounds, modeled by special quasirandom structures (SQS). The computed mechanical properties of these alloys enrich the database of hard coating materials, which may facilitate the experimental synthesis of such materials with appropriate material selection and design for hard coatings application.

2. Computational Methods

We performed first-principles computations based on density functional theory (DFT) using the Vienna *Ab initio* Simulation Package (VASP) [39-42]. The projector augmented wave (PAW) [43, 44] method was implemented with the Perdew-Burke-Ernzerhof (PBE) generalized gradient approximation (GGA) [45, 46]. Pseudo-potentials Ti_sv, Sc_sv and Y_sv, for which semi-core *s* and *p* electrons are treated as valence states, and the standard N pseudopotential were chosen from the VASP database [47]. A 400 eV kinetic energy cut-off was selected for the plane-wave basis set in the expansion of electron-wave functions. For all the structures, Monkhorst-Pack *k*-points meshes [48-51] were created with k-points per reciprocal atom (KPPRA) of density 4000. Electronic minimization was done with Gaussian smearing of width 0.1 eV by setting the convergence criterion to 10^{-5} eV/atom, whereas, ionic relaxation was performed using conjugate-gradient algorithm with a force criterion of 0.02 eV/Å. For the end members TiN, ScN and YN, we fit the computed energies of 5 volumes, varied about the estimated minimum, to the 3rd order Birch-Murnaghan [52, 53] equation of state, allowing accurate equilibrium energies, volumes, and bulk moduli to be obtained as described in earlier works [17-20, 54, 55].

The MIT *Ab initio* Phase Stability (maps) [56, 57] code from the Alloy Theoretic Automated Toolkit (ATAT) package [56-59] was used to generate the Cluster Expansion (CEs) and energy landscapes for $Ti_{1-x}Sc_xN$ and $Ti_{1-x}Y_xN$ alloy systems. Their phase diagrams were generated from the output of Monte Carlo simulations performed using Easy Monte Carlo Code (emc2 and phb) [58, 59] within ATAT. Phonon vibrational contributions were neglected.

To study the properties of random solid solution for these two alloy systems at varying atomic compositions, ranging from x = 0.125 to 0.875 in a step of 0.125, we generated special quasi-random structures (SQSs) [60-62] using the code sqs2tdb from ATAT. Each SQS contained 64 total atoms with 32 exchangeable metal sites. The SQSs were used to compute the elastic constants using the energy-strain method from two robust Python workflow packages; pyvasp-workflow [63] and pydass_vasp [64], each of which implement routines from Pymatgen [65]. To obtain the three independent elastic constants, C_{11}, C_{12} and C_{44} for these random solid solutions assuming symmetry of the cubic rocksalt system with space group $Fm\bar{3}m$, the pymatgen elasticity package was used. Elastic constants for the end members and predicted ground states were also calculated using the method of energy-strain, i.e., applying strains to the unit cell and then fitting the energies and strains to a second order polynomial as detailed in [17-20, 54, 55]. For the intermetallic structures, which exhibit slight deviation from cubic symmetry of the rocksalt system, the elastic constants were averaged arithmetically over the directions as described in [35, 103], i.e., C_{11}, C_{22} and C_{33} were averaged yielding $\bar{C}_{11}$, whereas, C_{44}, C_{55} and C_{66} were averaged yielding $\bar{C}_{44}$.

From these three independent elastic constants, other derived mechanical properties such as Bulk modulus (B), Shear modulus (G), Pugh's ratio (k), Poisson's ratio (v), Young's modulus (E) were calculated using the following equations.

$$B = (C_{11} + 2C_{12})/3. \qquad \text{Eq. (1)}$$

$$G_V = [(C_{11} - C_{12}) + 3C_{44}]/5, \qquad \text{Eq. (2)}$$

$$G_R = [5(C_{11} - C_{12})\, C_{44}]/(4C_{44} + 3C_{11} - 3C_{12}), \qquad \text{Eq. (3)}$$

$$G = (G_V + G_R)/2. \qquad \text{Eq. (4)}$$

$$k = G/B \qquad \text{Eq. (5)}$$

$$v = (3 - 2k)/[2(3+k)] \qquad \text{Eq. (6)}$$

$$E = 9G/(3+k). \qquad \text{Eq. (7)}$$

G_V and G_R are polycrystalline shear modulus in Voigt and Reuss approximation while G is their Hill's arithmetic mean. The Vickers hardness (H_V) of all structures in the $Ti_{1-x}Sc_xN$ and $Ti_{1-x}Y_xN$ alloy systems was calculated using the equation from Tian's model [66], given by,

$$H_V = 0.92k^{1.137}G^{0.708} \qquad \text{Eq. (8)}$$

To test for the mechanical (elastic) stability of all the calculated structures, the following stability criteria of Born [67, 68] was used,

$$C_{11} > C_{12},\ C_{11} + 2C_{12} > 0,\ C_{44} > 0 \qquad \text{Eq. (9)}$$

To observe any correlation between the hardness of the SQSs and the charge transfer from metal atoms to nitrogen atom, we utilized Bader charge analysis [69-72] with Bader's division scheme [73, 74] using Fast Fourier Transform (FFT) grids of 200×200×200. The local density of states (LDOS) for the predicted ground states and end member compounds were calculated with GGA using tetrahedron method with Blochl corrections [75]. To investigate detailed bonding characteristics, Crystal Orbital Hamiltonian Populations (COHP) were computed using the LOBSTER package [76-80].

3. Results and Discussions

3.1 Properties of end member compounds TiN, ScN, and YN

Calculated equilibrium lattice parameters, elastic constants (C_{11}, C_{12}, C_{44}), and derived moduli for the end member compounds are listed in Table 1. Experimental values, with which our data agrees, are also listed in Table 1 for comparison. TiN, ScN, and YN are found to exhibit volumes (per formula unit) of 19.2, 23.11, 19.53 in Å^3. These cell sizes are directly linked to ionic radii of the corresponding transition metals: Ti^{4+} (0.61 Å), Sc^{3+} (0.75 Å) and Y^{3+} (0.9 Å) [81]. The elastic constants C_{11} and C_{12} are inversely related to cell volume owing to the weakened stiffness of corresponding metal-nitrogen bonds at increased lengths. In contrast, C_{44} shows no clear correlation with volume, but is instead more closely related to underlying electronic properties, as will be discussed in the next paragraph. In agreement with previous works [17 -20], Vickers hardness (H_V) is shown to be strongly dependent on C_{44}, whereas C_{11} and C_{12} have only minor effects. The importance of C_{44} can be attributed to its shear-resistant nature, which is crucial to maintain high hardness within the rocksalt structure. Thus, TiN, ScN and YN all display high C_{44} values and hence good hardness H_V (24.2, 25.1 and 20.6 in GPa respectively), with ScN being the hardest compound among the three end members. These calculated values of hardness agree well with available experimental values [7, 93, 95]. Regarding the bulk (B), shear (G), and Young's moduli (E), anticorrelation with volume is observed, i.e., materials exhibiting greater density are more highly resistant to structural deformations. Hence, due to its relatively large volume, YN exhibits low bulk and shear moduli, leading to a low hardness of 20.6 GPa.

The mechanical properties of these end members, specifically C_{44} and hardness, can be explained through analysis of projected density of states (PDOS). As shown in Figure 1, clear splitting of the metal t_{2g} and e_g states is observed due to the octahedral ligand field within the rocksalt structure. For all end members, the bonding e_g orbitals are completely occupied and exhibit significant σ overlap with the N *p* orbitals as reflected by strong *d*-*p* hybridization at low energies in the PDOS. Occupation of the t_{2g} orbitals, which exhibit minimal bonding-antibonding splitting, is strongly dependent on the transition metal. As TiN is nominally d^1, it contributes one itinerant electron to the partially-filled t_{2g} manifold and is therefore metallic. In contrast, the d^0 configurations of ScN and YN cause them to be zero-gap semiconductors [98] within the framework of GGA. However, the effects of electron correlation, arising from the presence of strongly localized 3*d* orbitals, are known to enhance the band gap magnitudes to approximately 0.9 eV for each compound [99-101]. With respect to hardness, the t_{2g} and e_g orbitals play opposing roles, i.e., occupied e_g bonding orbitals are strongly resistant to shearing and compression whereas, occupied t_{2g} orbitals favor shearing due to enhanced σ overlap among second-nearest neighbor metal atoms [85]. Hence, the filled e_g bonding states and unfilled t_{2g} nonbonding states of ScN allows it to retain a shear modulus and hardness higher than that of TiN, in which the t_{2g} states are partially filled. However, *d-p* hybridization is weaker in ScN owing to the low electronegativity of Sc. As for YN, the discussed effects of enhanced covalent interaction are dominated by the large volume expansion as discussed previously, leading to decreased hardness. Therefore, to achieve maximum hardness, we aim to balance highly covalent metal-nitrogen bonds, low occupation of the t_{2g} states, and minimal volume expansion.

3.2 Energy landscapes and phase diagrams

Table S1 of the supplemental material summarizes the number of structures calculated with DFT, number of clusters (pairs, triplets and quadruplets) used, and cross-validation (CV) scores for the cluster expansion of $Ti_{1-x}Sc_xN$ and $Ti_{1-x}Y_xN$. Computed energy landscapes of the two quasi-binary systems, $Ti_{1-x}Sc_xN$ and $Ti_{1-x}Y_xN$, are displayed in Figure 2. We find that the mixture of TiN and YN is strongly endothermic and significant upward-bowing (concavity) is observed in the formation energies (ΔE_f) of all enumerated structures, with ΔE_f reaching values as high as 500 meV per atom. Such strong rise in enthalpy can be attributed to the large differences in the size, ionic radius, and electronegativity of Ti and Y [81, 82], causing structural distortions (to be discussed in section 3.4) and strain energy in the resulting mixtures. Ti and Y display electronegativities of 1.32 and 1.11 respectively. Hence, this difference will lead to enhanced charge transfer according to the relation for charge transferred per atom, ΔZ_Y, and the difference in electronegativity, $\Delta\phi$, ΔZ_Y, = (1.2) (1-c_Y) ($\Delta\phi$) [83], where c_Y is the concentration of Y within the alloy. See Figure S1 of the supplemental material. Greater charge transfer, as well as larger differences in ionic radii, lead to substantial changes in the volume as observed in Figure S2 of the supplemental material and therefore positive strain energy. As a result, the end members are the only stable ground states of this solid solution. However, contributions of configurational entropy to the Gibbs free energy of $Ti_{1-x}Y_xN$ may be significant enough to stabilize random solutions throughout intermediate concentrations. Due to large formation energies of the enumerated structures, a large miscibility gap can be expected for this system.

As opposed to $Ti_{1-x}Y_xN$, exothermic mixing is possible in $Ti_{1-x}Sc_xN$ due to the similarity of Ti and Sc in size, ionic radius, and electronegativity. The electronegativities of Ti and Sc, 1.32 and 1.2 respectively, are only slightly different; hence, only minor changes in charge transfer and volume occur as seen in Figures S1 and S2 of the supplemental material. This allows the effects of chemical bonding, controlled mostly by changes in valency, to lower the overall energy of the system [84]. As shown in Figure 2 (a), a decrease in formation energy with a downward-bowing (convexity) nature is observed for many enumerated structures at intermediate concentrations. We find four novel ground states which lie on the convex hull: $TiScN_2$, $TiSc_8N_9$, $TiSc_9N_{10}$, and $Ti_3Sc_2N_5$. Their formation energies are -17.968, -16.832, -15.264 and -17.987 in the units of meV respectively. All ground states are thermodynamically stable with $Ti_3Sc_2N_5$ being the most stable phase. As there are many enumerated structures exhibiting negative ΔE_f, disordering can be expected with the miscibility gaps closing at moderate temperatures.

The calculated phase diagram of $Ti_{1-x}Y_xN$ is displayed in Figure 3 (b). $Ti_{1-x}Y_xN$ features a miscibility gap far above the room temperature. For this system, the upper consolute temperature (T_c), above which complete miscibility is achieved, is predicted to be 7225 K. Considering that melting will almost surely occur below this temperature, we conclude that alloying in the $Ti_{1-x}Y_xN$ system may only be implemented at moderately low or high concentrations, for which configurational entropy dominates to allow solubility. In such a case, Y will diffuse into the grain boundaries and enhances the oxidation resistance and mechanical properties. Hence, the low solubility of YN provides opportunities to engineer hard coatings with segregated concentration variations as reported by Lewis *et al.* [104] and Choi *et al.* [105]. Detailed properties of these random solutions will be discussed in Section 3.3.

In Figure 3 (a), boundaries representing phase equilibria of the novel ground states and end members corresponding to the $Ti_{1-x}Sc_xN$ system are shown. We identify five major phase regions representing stability of unique heterogenous mixtures. Region I, representing the coexistence of TiN and $Ti_3Sc_2N_5$, covers a significant portion of the phase diagram; this indicates high tolerance of these phases with respect to variance in composition and temperature. More specifically, stability is maintained throughout Sc concentrations ranging from about 0 to 50% and temperatures ranging from 0 to 500 K. $Ti_3Sc_2N_5$ also coexists with $TiScN_2$ in region III near concentrations of 50% at moderately low temperatures. The strong stability of $Ti_3Sc_2N_5$ can be attributed to its low formation energy with respect to the other ground states. Coexisting at higher temperatures (500 to 660 K) and moderate Sc concentrations (0 to 50%) is the mixture of TiN and $TiScN_2$ owing to configurational entropy contributions of $TiScN_2$. Within this range of concentrations, the miscibility gap disappears above 660 K and complete miscibility is achieved. At higher Sc concentrations (> 50 %), significantly different properties are observed. $TiScN_2$ coexists with $TiSc_8N_9$ in region IV at Sc concentrations ranging from 50% to 90%. However, a random configuration becomes energetically favorable at a low temperature of about 225 K. In region V, characterized by stability of TiS_9cN_{10} and ScN, miscibility occurs at an even lower temperature of only 65 K. As will be discussed in greater detail in section 3.3, the low consolute temperature within this region of high Sc concentration can be attributed to the minimal formation energy difference between the SQSs and order ground states. Our result of computed upper consolute temperature of 660 K, where the miscibility gap completely disappears for all concentration of Sc in the $Ti_{1-x}Sc_xN$ quasy-binary system, compares well with the previous work of Kerdsongpanya *et al.* [37, 38], in which they have used first-principles calculations to predict a typical temperature of 800 °C (1073 K) at which $Sc_{1-x}Ti_xN$ changes its phase from ordered solid solution to disordered solid solution at x = 0.5. Our calculation also supports the experimental result of Gall *et al.* [102] in which they have demonstrated the synthesis of single-crystal rocksalt-structured $Ti_{1-x}Sc_xN$ epitaxial layers by reactive magnetron sputtering at 750 °C.

3.3 Properties of TiN-ScN intermediate phases

The intermetallics $TiScN_2$, $TiSc_8N_9$, $TiSc_9N_{10}$, $Ti_3Sc_2N_5$ are predicted to crystallize in rhombohedral, hexagonal, triclinic, and monoclinic symmetries respectively due to cation ordering. However, the rocksalt-type structure of the parent lattice is preserved in each case. Additionally, all structures are characterized by layering of Ti and Sc atoms, allowing strain energy to be minimized. Table 1 lists the lattice type, volume per nitrogen atom (V/N), three independent averaged elastic constants ($\bar{C}_{11}$, $\bar{C}_{12}$, $\bar{C}_{44}$) and derived moduli and constants for these intermediate phases, with detailed structures and lattice parameters provided in Figure S3 and Table S2 of the supplemental material. As only slight deviations from cubic symmetry occur due to cation ordering and lattice strain, a nearly-ideal symmetrized elastic tensor corresponding to cubic symmetry remains, i.e., components within the following groups are nearly equal: (i) C_{11}, C_{22}, and C_{33}, (ii) C_{44}, C_{55}, and C_{66} (iii) C_{12}, C_{13}, and C_{23}. Hence, average elastic constants ($\bar{C}_{11}$, $\bar{C}_{12}$, $\bar{C}_{44}$) are reported as discussed in the computational methods. Our results indicate that all four intermetallics, as with the end members, satisfy the mechanical stability criteria of Born [67, 68]. As listed in Table 1, high hardness is achieved in the intermediate phases as compared to the end members, with $Ti_3Sc_2N_5$ being the hardest compound (27.3 GPa). A mild anticorrelation between volume and hardness is observed for all phases. As shown in the phase diagram of $Ti_{1-x}Sc_xN$ system, $Ti_3Sc_2N_5$ is thermodynamically stable throughout a wide range of temperature from 0 K up to almost 500 K in the Sc composition ranging from 0 to 50 % as mentioned in previous section. Therefore, we suggest $Ti_3Sc_2N_5$ as a highly-suitable candidate for hard coating applications along with other three novel ground states as its competitors.

The high hardness of $Ti_3Sc_2N_5$ may be analyzed from a chemical and structural perspective. First, as shown in the PDOS in Figure 4, exceptionally strong *d-p* hybridization is observed throughout a wide range of energies (-7 eV to -2 eV), being directly associated with strong σ overlap of the metal $3d\ e_g$ orbitals with the nitrogen *p* orbitals. Further insight into the M-N bond strength is provided by the COHP curves in Figure 4, showing complete occupation of states with high bonding character. By integrating the COHP curves below the Fermi level, we obtain average M-N -IpCOHP and M-M -IpCOHP values for the end members as well as for the novel ground states and these values are listed in Table S3 of the supplementary material. The M-N -IpCOHP value of 1.721 eV for $Ti_3Sc_2N_5$ is significantly higher than that of the end member compounds, e.g., 1.415 eV and 1.428 eV for TiN and ScN respectively. Hence, greater covalent/directional character of these bonds leads to increased resistance to shearing and compression. Secondly, both the PDOS and COHP curves indicate decreased occupation of the metal t_{2g} orbitals, with respect to TiN, owing to the valence electron concentration (VEC) of $Ti_3Sc_2N_5$ (8.6) being less than that of TiN (9). As discussed previously, shear modulus is maximized when occupation of the t_{2g} states, which favor shearing due to metal-metal bonding, is minimized. Lastly, $Ti_3Sc_2N_5$ displays the lowest volume as seen from Table 1, and therefore highest density, of the intermetallic phases; thus, contributing further to its high hardness.

3.4 Effects of cation disorder

Formation energies of the fully-relaxed SQSs are displayed in Figure 2. For $Ti_{1-x}Y_xN$, these energies closely resemble the general trend of enumerated structures within the cluster expansion; significant upward-bowing is observed. Hence, the high consolute temperature of $Ti_{1-x}Y_xN$ can be attributed to the large and unfavorable difference between the formation energy of the SQSs at intermediate concentrations in comparison to those of the end members TiN and YN. As for $Ti_{1-x}Sc_xN$, the SQS formation energies are strongly dependent on composition. At low to intermediate Sc concentrations, the SQS energies lie about 20-30 meV/f.u. above those of the respective ground states, leading to miscibility at temperatures above 660 K. In contrast, the SQS energies at high Sc concentrations lie only slightly above (5-10 meV/f.u.) the convex hull, resulting in much lower consolute temperatures ranging from 65 to 225 K.

The energetics of these systems are closely related to their underlying structures. Figure 5 displays distributions of nearest-neighbor metal-nitrogen-metal bond angles within the SQSs of $Ti_{1-x}Sc_xN$ and $Ti_{1-x}Y_xN$. As expected, cation-disordering causes numerous atomic displacements to occur within each locally octahedral environment. For $Ti_{1-x}Y_xN$, these octahedral distortions become unusually large at intermediate concentrations, with individual bond angles varying by as much as 20°. Such major structural deviations, owing to the mismatch in ionic radii of Ti and Y, are known to enhance occupation of antibonding orbitals within octahedral ligand fields [86, 87] and therefore cause energetic instability within $Ti_{1-x}Y_xN$. As for $Ti_{1-x}Sc_xN$, for which the cation radii are more similar, only minor distortions take place, with bond angles generally lying within the range of 86°-94°. Hence, this causes only a relatively low rise in the formation energy for $Ti_{1-x}Sc_xN$. Interestingly, at high Sc concentrations, some degree of short-range order begins to emerge. This effect, which is indicated by grouping of bond angles above and below the ideal value of 90^o, accounts for the lowered SQS formation energy at high Sc concentrations as shown in the energy landscape of $Ti_{1-x}Sc_xN$ (Figure 2 (a)).

Elastic constants (C_{11}, C_{12} and C_{44}) and derived mechanical properties (bulk modulus, shear modulus, and Vickers hardness) of the SQSs are displayed in Figure 6 as a function of Sc and Y concentration for $Ti_{1-x}Sc_xN$ and $Ti_{1-x}Y_xN$ respectively, with detailed numeric values listed in Table S4 of the Supplementary Material. All the random solid solutions satisfy the mechanical stability criteria of Born [13, 14, 67, 68] as other compounds discussed previously. Our results show that bulk modulus, being directly related to C_{11}, and C_{12}, decreases at increased Sc and Y concentrations owing to volumetric expansion and decrease in metal-nitrogen bond length stiffness. Regarding C_{44} and the remaining moduli, significantly different behaviors are observed in $Ti_{1-x}Sc_xN$ and $Ti_{1-x}Y_xN$. In the latter, substantial weakening, reflected by decreases in shear moduli and hardness, occurs at higher Y concentrations. This result can be attributed to strong structural distortions, as well as the increase in spatial extent of the diffuse 4*d* orbitals contributed from Y, which are less shear-resistant than the strongly localized 3*d* orbitals of Ti. In contrast, $Ti_{1-x}Sc_xN$ exhibits an increase in C_{44}, and therefore in hardness, at intermediate concentrations. A maximum Vickers hardness of 27 GPa is found to occur at 62.5% atomic concentration of Sc, corresponding to a VEC of about 8.4. This result agrees with our earlier findings showing maximum hardness in the predicted intermetallic phase $Ti_3Sc_2N_5$ with intermediate VEC of 8.6. We also observe that the hardness of the random solution is very slightly lower (~0.3 GPa) than that of the ordered phase due to the enhanced structural distortions resulting from disorder.

Our findings regarding the correspondence of hardness with VEC indicate that the mechanical properties within $Ti_{1-x}Sc_xN$ are clearly influenced by electron valency. To further support this, the PDOS of the cation-disordered $Ti_{0.375}Sc_{0.625}N$ configuration is displayed in Figure S4 of the supplemental material. In a similar manner to $Ti_3Sc_2N_5$, exceptionally strong *d-p* hybridization, mediated by σ-overlap of the highly-localized 3*d* e_g and 2*p* orbitals, is observed through a wide range of energies (-6 eV to -2 eV) below the Fermi level. Additionally, relatively minimal occupation of the 3*d* t_{2g} orbitals occurs. Each of these factors contribute to the increased hardness of $Ti_{1-x}Sc_xN$ at the VEC of 8.4. These results agree well with the previously studied system of TiC_xN_{1-x}, which has been shown to exhibit maximum hardness at a VEC of 8.4 [7].

4. Conclusion

In summary, we have investigated the phase stability of two quasi-binary ceramic systems, $Ti_{1-x}Sc_xN$ and $Ti_{1-x}Y_xN$ ($0 \leq x \leq 1$) using first principles methods based on DFT, CE, and MC simulations. Owing to the similarity in the size, ionic radius, and electronegativity of Ti and Sc, a strong exothermic mixing is predicted in $Ti_{1-x}Sc_xN$, allowing the formation of four thermodynamically stable intermetallic phases: $TiScN_2$, $TiSc_8N_9$, $TiSc_9N_{10}$, and $Ti_3Sc_2N_5$. These novel compounds, for which stability is characterized in the phase diagram, are predicted to crystallize in layered rocksalt-type structures to minimize strain energy. Of these phases, $Ti_3Sc_2N_5$ uniquely maintains stability throughout a wide range of concentrations (0 to 50% Sc) and temperatures (0 to 500 K). In contrast to $Ti_{1-x}Sc_xN$, the system of $Ti_{1-x}Y_xN$ is found to exhibit strong endothermic mixing due to the large lattice mismatch between Ti and Y. Hence, solubility is achieved only at low/high Y concentrations or at very high temperatures (>7225 K).

We have characterized the mechanical properties of $Ti_{1-x}Sc_xN$ and $Ti_{1-x}Y_xN$, with the end members exhibiting Vickers hardness values of 24.2, 25.1, and 20.6 GPa respectively. The predicted intermetallics of the $Ti_{1-x}Sc_xN$ system are shown to display increased hardness with respect to the end members TiN and ScN. Of these compounds, $Ti_3Sc_2N_5$ achieves the highest hardness of 27.3 GPa. To compare these findings with the properties of the respective cation-disordered alloys occurring at high temperatures, we have studied the SQSs of $Ti_{1-x}Sc_xN$ and $Ti_{1-x}Y_xN$. The latter exhibits weakened mechanical properties due to significant volumetric expansion and decreased electron localization. In contrast, the former shows enhanced hardness, being directly related to an increase in C_{44}, at intermediate concentrations. A maximum hardness of about 27.0 GPa is achieved at a VEC of 8.4, which is in agreement with previous findings in related systems [7]. However, a slight decrease in hardness with respect to the ordered phases is observed due to structural distortions.

Lastly, to provide clear explanation of the trends in mechanical properties, we have studied the underlying electronic structure of $Ti_{1-x}Sc_xN$ and $Ti_{1-x}Y_xN$ using PDOS and COHP curves. Each system is characterized by strong hybridization of bonding character occurring at low energies, being related to σ-overlap of *d* e_g and 2*p* orbitals, and at higher energies some degree of (nearly) nonbonding *d* t_{2g} states, for which occupation may be tuned by changes in VEC. The e_g states contribute to high hardness due to their shear-resistant nature within the rocksalt structure, whereas t_{2g} states cause decreased hardness as they favor shearing owing to increased overlap with equivalent orbitals of the 2nd-nearest neighbors through metal-metal bonding. Hence, we find that hardness is maximized at intermediate Sc concentrations, corresponding to VEC ranging from 8.4-8.6, due to enhanced *d*-*p* hybridization and minimized t_{2g} occupation, shown by the PDOS and COHP curves of $Ti_3Sc_2N_5$ and $Ti_{0.375}Sc_{0.625}N$. In the case of $Ti_{1-x}Y_xN$, maximum hardness may not be achieved, as structural distortions and volumetric expansion dominate over electronic effects.

We conclude that the high hardness and robust thermal stability of the $Ti_{1-x}Sc_xN$ alloys make them promising candidates for improved hard coating applications. Moving forward, we suggest experimental synthesis by cathodic arc deposition or through reactive magnetron sputter deposition as previously demonstrated [88, 89]. In addition to the direct practical applications of this work, the methodology developed here could be applied to discover next-generation structural and functional alloys, with mechanical properties finely tuned through controlled electron valency, using a purely materials-by-design approach derived from first-principles.

Acknowledgements

The computing for this project was performed at the Ohio Supercomputer Center (OSC) [106]. We thank the CMMI from the National Science Foundation grants 1629239 and 1629230 for funding this work.

References:

[1] J.G. Zhao, S.J. You, L.X. Yang, C.Q. Jin, Structural phase transition of Cu_3N under high pressure, Solid State Commun. 150 (2010) 1521–1524, http://dx.doi.org/10. 1016/j.ssc.2010.06.012.

[2] S. Kodambaka, S.V. Khare, V. Petrova, D.D. Johnson, I. Petrov, J.E. Greene, Absolute orientation-dependent anisotropic TiN (111) island step energies and stiffnesses from shape fluctuation analyses, Phys. Rev. B 67 (2003), http://dx.doi. org/10.1103/PhysRevB.67.035409.

[3] S.H. Jhi, S.G. Louie, M.L. Cohen, J. Ihm, Vacancy hardening and softening in transition metal carbides and nitrides, Phys. Rev. Lett. 86 (2001) 3348–3351, http://dx.doi.org/10.1103/PhysRevLett.86.3348.

[4] S.H. Jhi, J. Ihm, S.G. Louie, M.L. Cohen, Electronic mechanism of hardness enhancement in transition-metal carbonitrides, Nature 399 (1999) 132–134, http:// dx.doi.org/10.1038/20148.

[5] A.Y. Liu, M.L. Cohen, Prediction of new low compressibility solids. Science 245 (1989) 841–842, http://dx.doi.org/10.1126/science.245.4920.841.

[6] X.J. Chen, V. V Struzhkin, Z.G. Wu, M. Somayazulu, J. Qian, S. Kung, A.N. Christensen, Y.S. Zhao, R.E. Cohen, H.K. Mao, R.J. Hemley, Hard superconducting nitrides, Proc. Natl. Acad. Sci. U. S. A 102 (2005) 3198–3201, http:// dx.doi.org/10.1073/pnas.0500174102.

[7] H. Holleck, Material selection for hard coatings, J. Vac. Sci. Technol. A Vacuum, Surfaces, Film 4 (1986) 2661, http://dx.doi.org/10.1116/1.573700.

[8] J.C. Crowhurst, Synthesis and characterization of the nitrides of platinum and iridium, Science (Wash. D C) 311 (2006) 1275–1278, http://dx.doi.org/10.1126/ science.1121813.

[9] E. Gregoryanz, C. Sanloup, M. Somayazulu, J. Badro, G. Fiquet, H.K. Mao, R.J. Hemley, Synthesis and characterization of a binary noble metal nitride, Nat. Mater. 3 (2004) 294–297, http://dx.doi.org/10.1038/nmat1115.

[10] J.A. Montoya, A.D. Hernandez, C. Sanloup, E. Gregoryanz, S. Scandolo, OsN_2: crystal structure and electronic properties, Appl. Phys. Lett. 90 (2007), http://dx. doi.org/10.1063/1.2430631.

[11] A.F. Young, C. Sanloup, E. Gregoryanz, S. Scandolo, R.J. Hemley, H.K. Mao, Synthesis of novel transition metal nitrides IrN_2 and OsN_2, Phys. Rev. Lett. 96 (2006) 1–4, http://dx.doi.org/10.1103/PhysRevLett.96.155501.

[12] J.C. Crowhurst, A.F. Goncharov, B. Sadigh, J.M. Zaug, D. Aberg, Y. Meng, V.B. Prakapenka, Synthesis and characterization of nitrides of iridium and palladium, J. Mater. Res. 23 (2008) 1–5, http://dx.doi.org/10.1557/jmr.2008.0027.

[13] S.K.R. Patil, S.V. Khare, B.R. Tuttle, J.K. Bording, S. Kodambaka, Mechanical stability of possible structures of PtN investigated using first-principles calculations, Phys. Rev. B Condens. Matter 73 (2006) 1–8, http://dx.doi.org/10.1103/ PhysRevB.73.104118.

[14] S.K.R. Patil, N.S. Mangale, S.V. Khare, S. Marsillac, Super hard cubic phases of period VI transition metal nitrides: first principles investigation, Thin Solid Films 517 (2008) 824–827, http://dx.doi.org/10.1016/j.tsf.2008.07.034.

[15] W. Chen, J.Z. Jiang, Elastic properties and electronic structures of 4d- and 5d transition metal mononitrides, J. Alloy. Comp. 499 (2010) 243–254, http://dx.doi. org/10.1016/j.jallcom.2010.03.176.

[16] E.J. Zhao, J.P. Wang, J. Meng, Z.J. Wu, Structural, mechanical and electronic properties of 4d transition metal mononitrides by first-principles, Comput. Mater. Sci. 47 (2010) 1064–1071, http://dx.doi.org/10.1016/j.commatsci.2009.12.011.

[17] Z.T.Y. Liu, X. Zhou, S.V. Khare, D. Gall, Structural, mechanical and electronic properties of 3d transition metal nitrides in cubic zincblende, rocksalt and cesium chloride structures: a first-principles investigation, J. Phys. Condens. Matter 26 (2014) 25404, http://dx.doi.org/10.1088/0953-8984/26/2/025404.

[18] Z.T.Y. Liu, X. Zhou, D. Gall, S.V. Khare, First-principles investigation of the structural, mechanical and electronic properties of the NbO-structured 3d, 4d and 5d transition metal nitrides, Comput. Mater. Sci. 84 (2014) 365–373, http://dx. doi.org/10.1016/j.commatsci.2013.12.038.

[19] X. Zhou, D. Gall, S.V. Khare, Mechanical properties and electronic structure of anti-ReO_3 structured cubic nitrides, M_3N, of d block transition metals M: an *ab initio* study, J. Alloy. Comp. 595 (2014) 80–86, http://dx.doi.org/10.1016/j. jallcom.2014.01.116.

[20] V. Adhikari, Z.T.Y. Liu, N.J. Szymanski, I. Khatri, D. Gall, P. Sarin, S.V. Khare, First-principles study of mechanical and magnetic properties of transition metal (M) nitrides in the cubic M_4N structure, Journal of Physics and Chemistry of Solids 120 (2018) 197–206, https://doi.org/10.1016/j.jpcs.2018.04.043.

[21] K. Balasubramanian, S. Khare and D. Gall, Vacancy-induced mechanical stabilization of cubic tungsten nitride, Phys. Rev. B 94 (2016) 174111, DOI: 10.1103/PhysRevB.94.17411.

[22] L. Chen, Y. Gu, L. Shi, J. Ma, Z. Yang, Y. Qian, A Room-Temperature Synthesis of Titanium Nitride Hollow Spheres, J. Nanosci. Nanotechnol. 4 (2004) 896-898, https://doi.org/10.1166/jnn.2004.115.

[23] G. V. White, K. J. D. Mackenzie, J. H. Johnston, Carbothermal Synthesis of Titanium Nitride, Journal of Materials Science 27 (1992) 4287-4293, https://doi.org/10.1007/BF00541554.

[24] L.E. Toth, Transition Metal Carbides and Nitrides, Academic Press, New York, 1971.

[25] H. Kindlund, D.G. Sangiovanni, L. Martínez-De-Olcoz, J. Lu, J. Jensen, J. Birch, I. Petrov, J.E. Greene, V. Chirita, L. Hultman, Toughness enhancement in hard ceramic thin films by alloy design, Apl. Mater. 1 (2013) 42104, https:// doi.org/10.1063/1.4822440.

[26] D. G. Sangiovanni, V. Chirita, and L. Hultman, Electronic mechanism for toughness enhancement in $Ti_xM_{1-x}N$ (M=Mo and W), Phys. Rev. B 81 (2010) 104107, https://doi.org/10.1103/PhysRevB.81.104107.

[27] D.G. Sangiovanni, L. Hultman, and V. Chirita, Supertoughening in B1 transition metal nitride alloys by increased valence electron concentration, Acta Mater. 59 (2011) 2121, https://doi.org/10.1016/j.actamat.2010.12.013.

[28] Z.T.Y. Liu, B.P. Burton, S.V. Khare and D. Gall, First-principles phase diagram calculations for the rocksalt-structure quasibinary systems TiN–ZrN, TiN–HfN and ZrN–HfN, J. Phys.: Condens. Matter 29 (2017) 035401 (11pp), https://doi.org/10.1088/0953-8984/29/3/035401.

[29] V. Petrman, J. Houska, Trends in formation energies and elastic moduli of ternary and quaternary transition metal nitrides, Journal of Materials Science, 48 (2013) 21, https://doi.org/10.1007/s10853-013-7582-4.

[30] G.M. Matenoglou, L.E Koutsokeras, Ch.E. Lekka, G. Abadias, C. Kosmidis, G.A. Evangelakis, P. Patsalas, Structure, stability and bonding of ternary transition metal nitrides, Surface & Coatings Technology 204 (2009) 911–914, https://doi.org/10.1016/j.surfcoat.2009.06.032.

[31] K. Vasu, M. Ghanashyam Krishna, K. A. Padmanabhan, Effect of Nb concentration on the structure, mechanical, optical, and electrical properties of nano-crystalline $Ti_{1-x}Nb_xN$ thin films, J Mater Sci (2012) 47:3522–3528, https://doi.org/10.1007/s10853-011-6197-x.

[32] P. Djemia, M. Benhamida, Kh. Bouamama, L. Belliard, D. Faurie, G. Abadias, Structural and elastic properties of ternary metal nitrides $Ti_xTa_{1-x}N$ alloys: First-principles calculations versus experiments, Surface & Coatings Technology 215 (2013) 199–208, http://dx.doi.org/10.1016/j.surfcoat.2012.09.059.

[33] G. M. Matenoglou, Ch. E. Lekka, L. E. Koutsokeras, G. Karras, C. Kosmidis, G. A. Evangelakis, and P. Patsalas, Structure and electronic properties of conducting, ternary $Ti_xTa_{1-x}N$films, Journal of Applied Physics 105 (2009), 103714, https://doi.org/10.1063/1.3131824.

[34] G. Abadias, V.I. Ivashchenko, L. Belliard, Ph. Djemia, Structure, phase stability and elastic properties in the $Ti_{1-x}Zr_xN$ thin-film system: Experimental and computational studies, Acta Materialia 60 (2012) 5601–5614, http://dx.doi.org/10.1016/j.actamat.2012.07.014.

[35] K. Balasubramanian, S.V. Khare and D. Gall, Valence electron concentration as an indicator for mechanical properties in rocksalt structure nitrides, carbides and carbonitrides, Acta Materialia, 152 (2018), 175-185, https://doi.org/10.1016/j.actamat.2018.04.033.

[36] B. Saha, S.K. Lawrence, J.L. Schroeder, J. Birch, D.F. Bahr, and T.D. Sands, Enhanced Hardness in Epitaxial TiAlScN Alloy Thin Films and Rocksalt TiN/(Al, Sc)N Superlattices, Applied Physics Letters, 105 (2014) 15 151904, http://dx.doi.org/10.1063/1.4898067.

[37] S. Kerdsongpanya, B. Alling, and P. Eklund, Phase stability of ScN-based solid solutions for thermoelectric applications from first principles calculations, J. Appl. Phys. 114 (2013) 073512; https://doi.org/10.1063/1.4818415.

[38] P. Eklund, S. Kerdsongpanya and B. Alling, Transition-metal-nitride-based thin films as novel energy harvesting materials, Journal of Materials Chemistry C 4 (2016) 3905-3914, https://doi.org/10.1039/c5tc03891j.

[39] G. Kresse, J. Furthmuller, Efficient iterative schemes for *ab initio* total-energy calculations using a plane-wave basis set, Phys. Rev. B 54 (1996) 11169–11186, http://dx.doi.org/10.1103/PhysRevB.54.11169.

[34] G. Kresse, J. Furthmuller, Efficiency of ab-initio total energy calculations for metals and semiconductors using a plane-wave basis set, Comput. Mater. Sci. 6 (1996) 15–50, http://dx.doi.org/10.1016/0927-0256(96)00008-0.

[41] G. Kresse, J. Hafner, *Ab initio* molecular-dynamics simulation of the liquid-metal–amorphous-semiconductor transition in germanium, Phys. Rev. B 49 (1994) 14251–14269, http://dx.doi.org/10.1103/PhysRevB.49.14251.

[42] G. Kresse, J. Hafner, *Ab initio* molecular dynamics for liquid metals, Phys. Rev. B 47 (1993) 558–561, http://dx.doi.org/10.1103/PhysRevB.47.558.

[43] P.E. Blöchl, Projector augmented-wave method, Phys. Rev. B 50 (1994) 17953–17979, http://dx.doi.org/10.1103/PhysRevB.50.17953.

[44] G. Kresse, D. Joubert, From ultrasoft pseudopotentials to the projector augmented-wave method, Phys. Rev. B 59 (1999) 1758–1775, http://dx.doi.org/10.1103/ PhysRevB.59.1758.

[45] J.P. Perdew, K. Burke, M. Ernzerhof, Generalized gradient approximation made simple, Phys. Rev. Lett. 77 (1996) 3865–3868, http://dx.doi.org/10.1103/ PhysRevLett.77.3865.

[46] J.P. Perdew, K. Burke, M. Ernzerhof, Generalized gradient approximation made simple, Phys. Rev. Lett. 78 (1997) 1396, https://link.aps.org/doi/10.1103/PhysRevLett.78.1396.

[47] G. Kresse, Recommended PAW Potentials for DFT Calculations Using vasp.5.2, (n. d.)

[48] H.J. Monkhorst, J.D. Pack, Special points for brillouin-zone integrations, Phys. Rev. B 13 (1976) 5188–5192, http://dx.doi.org/10.1103/PhysRevB.13.5188.

[49] J.D. Pack, H.J. Monkhorst, Special points for Brillioun-zone integrations - reply, Phys. Rev. B 16 (1977) 1748–1749, http://dx.doi.org/10.1103/PhysRevB.16. 1748.

[50] S.V. Khare, R.V. Kulkarni, D. Stroud, J.W. Wilkins, Energetics and bias-dependent scanning tunneling microscopy images of Si ad-dimers on Ge(001), Phys. Rev. B 60 (1999) 4458–4461, http://dx.doi.org/10.1103/Physrevb.60.4458.

[51] J.A. Warner, S.K.R. Patil, S.V. Khare, K.C. Masiulaniec, *Ab initio* calculations for properties of MAX phases Ti_2TlC, Zr_2TlC, and Hf_2TlC, Appl. Phys. Lett. 88 (2006) 101911, http://dx.doi.org/10.1063/1.2182009.

[52] F. Birch, Finite elastic strain of cubic crystals, Phys. Rev. 71 (1947) 809–824 http://link.aps.org/doi/10.1103/PhysRev.71.809.

[53] F. Birch, Finite strain isotherm and velocities for single-crystal and polycrystalline Nacl at high-pressures and 300° K, J. Geophys. Res. 83 (1978) 1257–1268, http://dx.doi.org/10.1029/Jb083ib03p01257.

[54] Z.T.Y. Liu, D. Gall, S.V. Khare, Electronic and bonding analysis of hardness in pyrite-type transition-metal pernitrides, Phys. Rev. B 90 (2014), DOI:10.1103/PhysRevB.90.134102 134102.

[55] I. Efthimiopoulos, I. Khatri, Z.T.Y. Liu, S.V. Khare, P. Sarin, V. Tsurkan, A. Loidl, D. Zhang and Y. Wang, Universal link of magnetic exchange and structural behavior under pressure in chromium spinels, Phys. Rev. B 97 (2018) 184435, DOI: 10.1103/PhysRevB.97.184435.

[56] A. van de Walle, M. Asta and G. Ceder, The alloy theoretic automated toolkit: a user guide CALPHAD Comput. Coupling Phase Diagr. Thermochem., 26 (2002) 539-553, 10.1016/S0364-5916(02)80006-2.

[57] A. van de Walle, Multicomponent multisublattice alloys, nonconfigurational entropy and other additions to the alloy theoretic automated toolkit CALPHAD, Comput. Coupling Phase Diagr. Thermochem. 33 (2009) 266–78, https://doi.org/10.1016/j.calphad.2008.12.005.

[58] A. van de Walle and M. Asta, Self-driven lattice-model Monte Carlo simulations of alloy thermodynamic properties and phase diagrams Model. Simul. Mater. Sci. Eng. 10 (2002) 521–538, 10.1088/0965-0393/10/5/304.

[59] A. van de Walle and G. Ceder, Automating first-principles phase diagram calculations J. Phase Equilib. 23 (2002) 348–359.

[60] A. Zunger, S.H. Wei, L.G. Ferreira and J.E. Bernard, Special quasirandom structures Phys. Rev. Lett. 65 (1990) 353–356, 10.1103/PhysRevLett.65.353.

[61] S.H. Wei, L.G. Ferreira, J.E. Bernard and A. Zunger, Electronic-properties of random alloys—special quasirandom structures, Phys. Rev. B 42 (1990) 9622–9649, 10.1103/PhysRevB.42.9622.

[62] A. van de Walle *et al.*, Efficient stochastic generation of special quasirandom structures CALPHAD, Comput. Coupling Phase Diagr. Thermochem. 42 (2013) 13–8, https://doi.org/10.1016/j.calphad.2013.06.006.

[63] Z.T.Y. Liu, 2016, pyvasp-workflow, a simple yet flexible programmatic workflow of describing, submitting and analyzing VASP jobs https://github.com/terencezl/ pyvasp-workflow.

[64] Z.T.Y. Liu, pydass_vasp, convenient Python modules and wrapping executable scripts, https://github.com/terencezl/pydass_vasp, (2015)

[65] S.P. Ong, W.D. Richards, A. Jain, G. Hautier, M. Kocher, S. Cholia, D. Gunter, V.L. Chevrier, K.A. Persson, G. Ceder, Python Materials Genomics (pymatgen): a robust, open-source python library for materials analysis, Comput. Mater. Sci. 68 (2013) 314–319, http://dx.doi.org/10.1016/j.commatsci.2012.10.028.

[66] Y. Tian, B. Xu, Z. Zhao, Microscopic theory of hardness and design of novel superhard crystals, Int. J. Refract. Metals Hard Mater. 33 (2012) 93–106, http://dx. doi.org/10.1016/j.ijrmhm.2012.02.021.

[67] J.F. Nye, Physical Properties of Crystals: Their Representation by Tensors and Matrices, Clarendon Press, 1985, http://books.google.com/books?id=ugwqluVB44C.

[68] F. Mouhat, F.-X. Coudert, Necessary and sufficient elastic stability conditions in various crystal systems, Phys. Rev. B 90 (2014) 224104, http://dx.doi.org/10. 1103/PhysRevB.90.224104.

[69] W. Arnaldsson Tang Chill, S. Henkelman, G.A, Bader. Charge Analysis, (n.d.). http://theory.cm.utexas.edu/bader/.

[70] G. Henkelman, A. Arnaldsson, H. Jonsson, A fast and robust algorithm for Bader decomposition of charge density, Comput. Mater. Sci. 36 (2006) 354–360, http:// dx.doi.org/10.1016/j.commatsci.2005.04.010.

[71] E. Sanville, S.D. Kenny, R. Smith, G. Henkelman, Improved grid-based algorithm for Bader charge allocation, J. Comput. Chem. 28 (2007) 899–908, http://dx.doi. org/10.1002/jcc.20575.

[72] W. Tang, E. Sanville, G. Henkelman, A grid-based Bader analysis algorithm without lattice bias, J. Phys. Condens. Matter 21 (2009) 84204, http://dx.doi.org/ 10.1088/0953-8984/21/8/084204.

[73] R.F.W. Bader, Atoms in Molecules: A Quantum Theory, Oxford University Press, New York, 1990.

[74] F.W. Bieglerkonig, R.F.W. Bader, T.H. Tang, Calculation of the average properties of atoms in molecules .2, J. Comput. Chem. 3 (1982) 317–328, http://dx.doi.org/ 10.1002/Jcc.540030306.

[75] P.E. Blöchl, O. Jepsen, O.K. Andersen, Improved tetrahedron method for brillouinzone integrations, Phys. Rev. B 49 (1994) 16223–16233, http://dx.doi.org/10. 1103/PhysRevB.49.16223.

[76] R. Dronskowski and P. E. Bloechl, Crystal Orbital Hamilton Populations (COHP): energy-resolved visualization of chemical bonding in solids based on density-functional calculations, The Journal of Physical Chemistry 97 (1993) (33), 8617-8624, DOI: 10.1021/j100135a014.

[77] V. L. Deringer, A. L. Tchougreeff and R. Dronskowski, Crystal Orbital Hamilton Populations (COHP) Analysis as Projected from Plane-Wave Basis Sets, J. Phys. Chem. A 115 (2011) 5461, DOI: 10.1021/jp202489s.

[78] S. Maintz, V. L. Deringer, A. L. Tchougreeff and R. Dronskowski, Analytic projection from plane-wave and PAW wavefunctions and application to chemical-bonding analysis in solids, J. Comput. Chem. 34 (2013) 2557, doi: 10.1002/jcc.23424.

[79] S. Maintz, V. L. Deringer, A. L. Tchougr´eeff and R. Dronskowski, LOBSTER: A Tool to Extract Chemical Bonding from Plane-Wave Based DFT, J. Comput. Chem. 37 (2016) 1030, DOI: 10.1002/jcc.24300.

[80] S. Maintz, M. Esser and R. Dronskowski, Efficient Rotation Local Basis Functions Using Real Spherical Harmonics, Acta Phys. Pol. B 47 (2016) 1165, DOI:10.5506/APhysPolB.47.1165.

[81] R.D. Shannon, Revised effective ionic radii and systematic studies of interatomic distances in halides and chalcogenides, Acta Crystallogr. A 32 (1976) 751–767, https://doi.org/10.1107/S0567739476001551.

[82] A.L. Allred, E.G. Rochow, A scale of electronegativity based on electrostatic force, J. Lnorg. Nucl. Chem. 5 (1958) 264–268, https://doi.org/10.1016/0022-1902(58)80003-2.

[83] A. R. Miedema, The Electronegativity Parameter for Transition Metals: Heat of Formation and Charge Transfer in Alloys, Journal of Less-Common Metals, 32 (1973) 117-136, https://doi.org/10.1016/0022-5088(73)90078-7.

[84] A. Pratap, M. Rani, and N. S. Saxena, Transfer of charge in liquid alloys, Pramana - J Phys 30 (1988) 239-244, https://doi.org/10.1007/BF02846698.

[85] L. Benco, Metal-to-Metal Bonding in Transition Metal Monocarbides and Mononitrides, Journal of Solid State Chemistry, 128 (1997) 121-129, DOI: 10.1006/jssc.1996.7184.

[86] N.J. Szymanski, L.N. Walters, O. Hellman, D. Gall, S.V. Khare, Dynamical Stabilization in Delafossite Nitrides for Solar Energy Conversion, Journal of Materials Chemistry A 6 (2018), 20852-20862, DOI: 10.1039/C8TA07536K.

[87] N.J. Szymanski, Z.T.Y. Liu, T. Alderson, N.J. Podraza, P. Sarin and S.V. Khare, Electronic and optical properties of vanadium oxides from first principles, Computational Materials Science 146 (2018), 310-318, https://doi.org/10.1016/j.commatsci.2018.01.048.

[88] D. Gall, I. Petrov, and J. E. Greene, Epitaxial $Sc_{1-x}Ti_xN$ (001): Optical and electronic transport properties, Journal of Applied Physics 89 (2001) 401, doi: 10.1063/1.1329348.

[89] F.J. DiSalvo, and S.J. Clarke, Ternary nitrides: a rapidly growing class of new materials, Current Opinion in Solid State & Materials Science 1 (1996), 241-249.

[90] T. Yoshida, A. Kawasaki, K. Nakagawa, K. Akashi, The synthesis of ultrafine titanium nitride in an r.f. plasma, Journal of Materials Science 14 (1979) 1624-1630, https://doi.org/10.1007/BF00569282.

[91] Powder Diffraction Files: 03-065-0565 (TiN), 00-035-0753 (ZrN), 00-033-0592 (HfN), (International Center for Diffraction Data) PDF-2 www.icdd.com/products/pdf2.htm.

[92] J. O. Kim, J. D. Achenbach, P. B. Mirkarimi, M. Shinn, and S. A. Barnett, Elastic constants of single-crystal transition-metal nitride films measured by line-focus acoustic microscopy, Journal of Applied Physics 72, 1805 (1992); https://doi.org/10.1063/1.351651.

[93] D. Gall, I. Petrov, N. Hellgren, L. Hultman, J. E. Sundgren, and J. E. Greene, Growth of poly- and single-crystal ScN on MgO(001): Role of low-energy N_2^+irradiation in determining texture, microstructure evolution, and mechanical properties, Journal of Applied Physics 84, 6034 (1998); https://doi.org/10.1063/1.368913.

[94] D. Gall, I. Petrov, P. Desjardins, and J. E. Greene, Microstructural evolution and Poisson ratio of epitaxial ScN grown on TiN(001)/MgO(001) by ultrahigh vacuum reactive magnetron sputter deposition, Journal of Applied Physics 86, 5524 (1999); https://doi.org/10.1063/1.371555.

[95] C.S. Shin, D. Gall, N. Hellgren, J. Patscheider, I. Petrov, J.E. Greene, Vacancy hardening in single-crystal TiNx(001) layers, J. Appl. Phys. 93 (2003) 6025–6028, http://dx.doi.org/10.1063/1.1568521.

[96] S. Bellucci, S. Bini, F. Micciulla, A. Dinescu, M. Danila, Synthesis of Titanium Nitride Film by RF Sputtering, Nanoscience and Nanotechnology Letters 3 (2011) 6 856-864, https://doi.org/10.1166/nnl.2011.1251.

[97] Her, Shiuh-Chuan; Wu, Cheng-Lin Fabrication and Characterization of Magnetron Sputtered Titanium Nitride Thin Film, Advanced Science Letters, 8 (2012) 200-204(5), DOI: https://doi.org/10.1166/asl.2012.2346.

[98] Y.F. Lu, H. Kono, T.I. Larkin, A.W. Rost, T. Takayama, A.V. Boris, B. Keimer & H. Takagi, Zero-gap semiconductor to excitonic insulator transition in Ta_2NiSe_5, Nature Communications 8 (2017) 14408, DOI: 10.1038/ncomms14408.

[99] R.P. Deng, B. Ozsdolay, P.Y. Zheng, S.V. Khare, and D. Gall, Optical and transport measurement and first-principles determination of the ScN band gap, Phys. Rev. B 90 (2015) 045104, DOI: 10.1103/PhysRevB.91.045104.

[100] C. Stampfl, W. Mannstadt, R. Asahi, and A. J. Freeman, Electronic structure and physical properties of early transition metal mononitrides: Density-functional theory LDA, GGA, and screened-exchange LDA FLAPW calculations, Phys. Rev. B 63 (2001) 155106 (2), DOI: https://doi.org/10.1103/PhysRevB.63.155106.

[101] B. Saha, T. D. Sands, and U. V. Waghmare, Electronic structure, vibrational spectrum, and thermal properties of yttrium nitride: A first principles study, J. Appl. Phys.109 (2011), 073720, DOI: 10.1063/1.3561499.

[102] D. Gall, M. Stoehr, and J.E. Greene, Vibrational modes in epitaxial $Ti_{1-x}Sc_xN$ (001) layers: An *ab initio* calculation and Raman spectroscopy study, Phys. Rev. B, 64 (2001) 174302, DOI:10.1103/PhysRevB.64.174302.

[103] M. Moakher, A.N. Norris, The closest elastic tensor of arbitrary symmetry to an elasticity tensor of lower symmetry, J. Elasticity 85 (2006) 215-263, https://doi.org/10.1007/s10659-006-9082-0.
[104] D. B. Lewis, L. A. Donohue, M. Lembke, W. D. Munz, R. Kuzel, V. Valvoda, and C. J. Blomfield, The influence of the yttrium content on the structure and properties of $Ti_{1-x-y-z}Al_xCr_yY_zN$ PVD hard coatings, Surf. Coat. Technol. 114 (1999) 187.

[105] W. S. Choi, S. K. Hwang, and C. M. Lee, Microstructure and chemical state of $Ti_{1-x}Y_xN$ film deposited by reactive magnetron sputtering, J. Vac. Sci. Technol. A 18 (2000) 2914, DOI: 10.1116/1.1319680.

[106] Ohio Supercomputer Center, (n.d.). http://osc.edu/ark:/19495/f5s1ph73.

Table 1

Table 1. Lattice constant (*a*), volume per formula unit (*V*/f. u.), elastic constants (C_{11}, C_{12}, C_{44}), Bulk modulus (*B*), Shear modulus (*G*), Pugh's ratio (*k*), Poisson's ratio (*v*), Young's modulus (*E*) and Vickers hardness (H_V) of the three end member compounds and the predicted four novel ground states. For the four intermetallic phases, volume per nitrogen atom (V/N) is provided for comparison.

End Members	*a* (Å)	V/f. u. (Å^3)	C_{11} (GPa)	C_{12} (GPa)	C_{44} (GPa)	*B* (GPa)	*G* (GPa)	*k*	*N*	*E* (GPa)	H_V (GPa)
TiN	4.25 4.245[a] 4.21[e]	19.19 19.1[b]	563.2	113.1	158.6	263.1 318[b]	182.5	0.69	0.22	444.7 590[c]	24.2 20.2[f] 21[g]
ScN	4.52 4.501[d] 4.52[e]	23.11	389.5	104.2	166.8	199.3 182 ± 40[d]	156.7	0.79	0.19	372.5 388 ± 20[d]	25.1 24.4 ± 1.3[d]
YN	4.91	29.53	318.5	76.8	122.6	157.4	121.9	0.77	0.19	290.7	20.6
Intermetallics	Lattice Type	V/ N (Å^3)	$\bar{C}_{11}$ (GPa)	$\bar{C}_{12}$ (GPa)	$\bar{C}_{44}$ (GPa)	*B* (GPa)	*G* (GPa)	*k*	*N*	*E* (GPa)	H_V (GPa)
$TiScN_2$	Rhombohedral	20.57	483.4	135.4	186.5	251.4	181.4	0.72	0.21	438.7	25.2
$TiSc_8N_9$	Hexagonal	22.14	440.7	112.5	164.7	221.9	164.5	0.74	0.2	395.6	24.3
$TiSc_9N_{10}$	Triclinic	22.21	444	104.3	168.6	217.5	169.1	0.78	0.19	402.8	26.1
$Ti_3Sc_2N_5$	Monoclinic	20.51	488.6	125.1	190.5	246.3	186.9	0.76	0.2	447.6	27.3

[a] Expt. from [90]
[b] Expt. from [91]
[c] Expt. from [92]
[d] Expt. from [93]
[e] Expt. from [94]
[f] Expt. from [95]
[g] Expt. from [7]

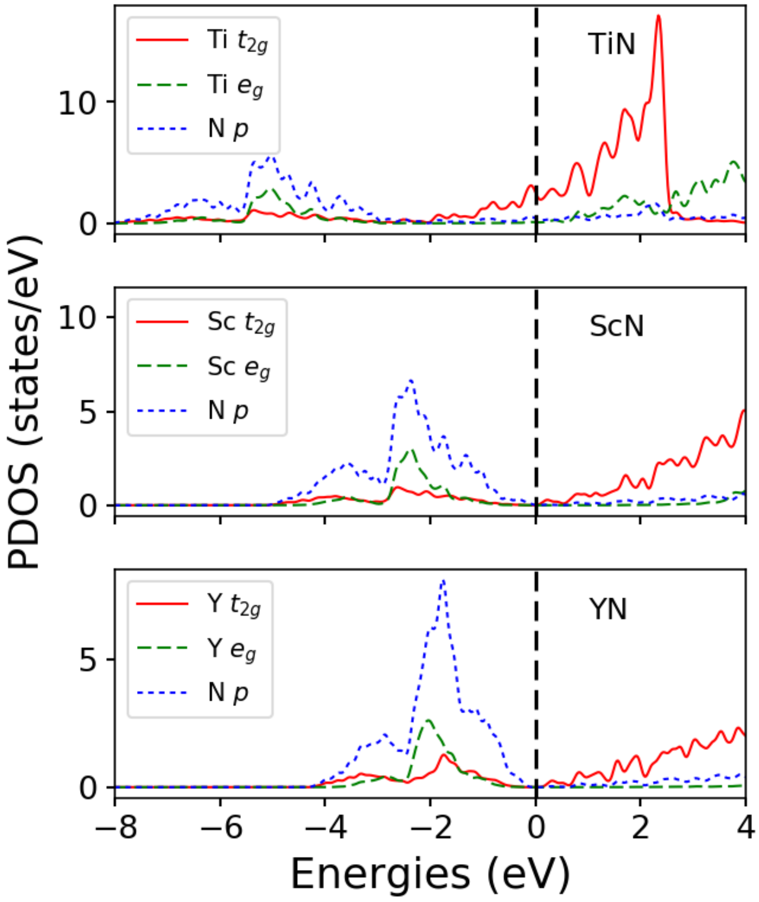

Figure 1. Projected density of states (PDOS) of the end member compounds TiN, ScN and YN. The Fermi energy is set to zero in each panel. Red solid and green long-dashed lines represent the metallic t_{2g} and e_g states respectively while blue short-dashed lines indicate nitrogen p states.

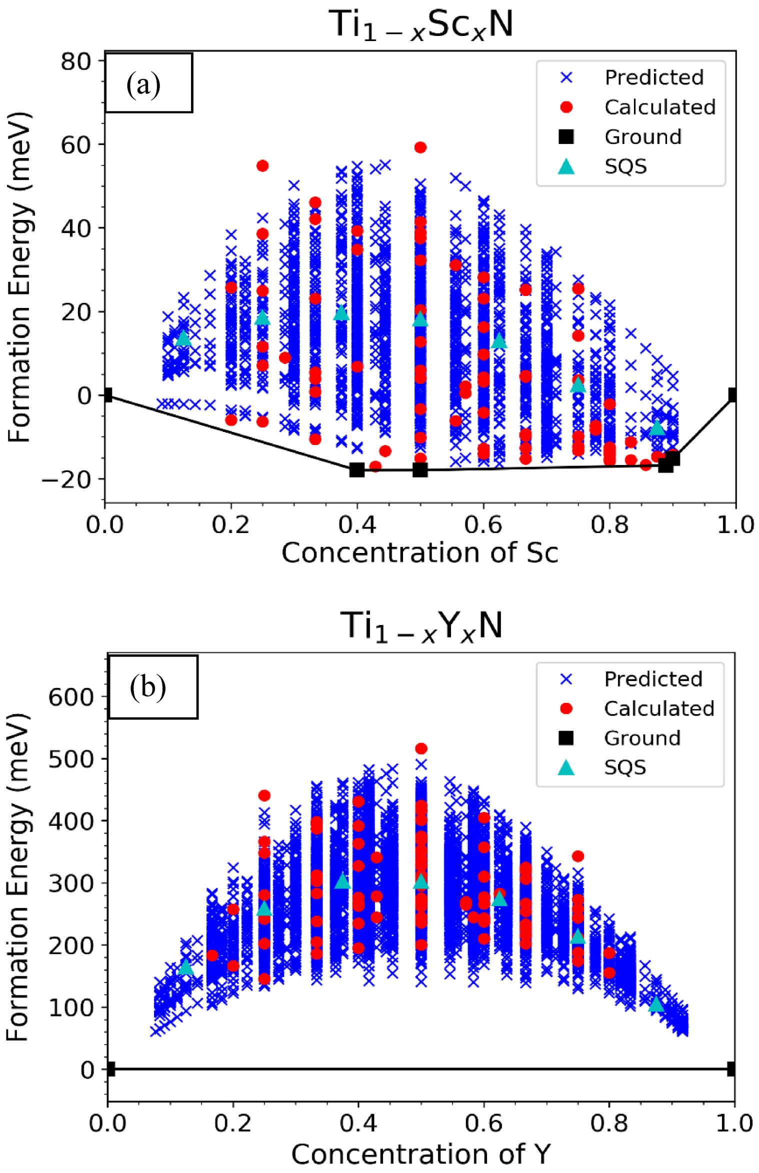

Figure 2. Formation energy per formula unit of (a) $Ti_{1-x}Sc_xN$ and (b) $Ti_{1-x}Y_xN$. Blue crosses indicate structures enumerated by CE, red circles represent structures calculated directly by DFT, black squares correspond to predicted ground states, and cyan triangles represent the SQSs.

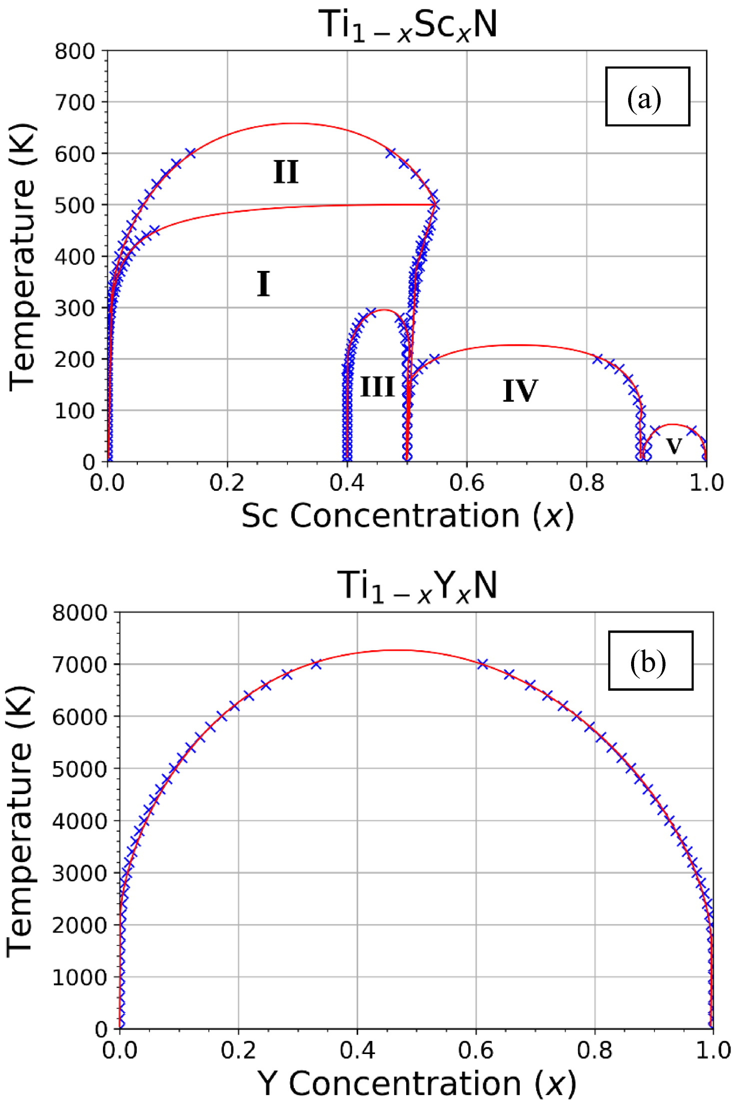

Figure 3. Calculated phase diagrams of (a) $Ti_{1-x}Sc_xN$ and (a) $Ti_{1-x}Y_xN$. Blue crosses represent data points computed directly from Monte Carlo methods, whereas red lines indicate interpolations and extrapolations of this data. Regions for the $Ti_{1-x}Sc_xN$ phase diagram are discussed in section 3.2.

Figure 4

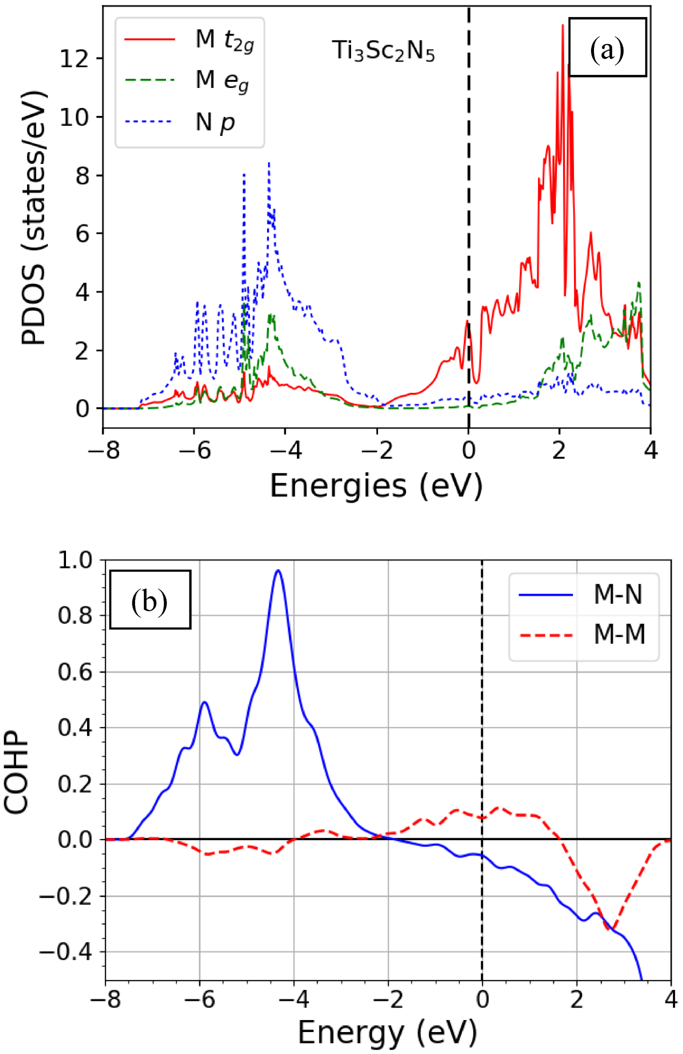

Figure 4. (a) Projected density of states and (b) Crystal Orbital Hamiltonian Populations (COHP) for the predicted intermetallic $Ti_3Sc_2N_5$ having the highest hardness. M-N and M-M represents metal-metal and metal-nitrogen interactions respectively. Positive and negative values (of COHP) correspond to bonding and antibonding respectively. The Fermi energy is set to zero in each panel.

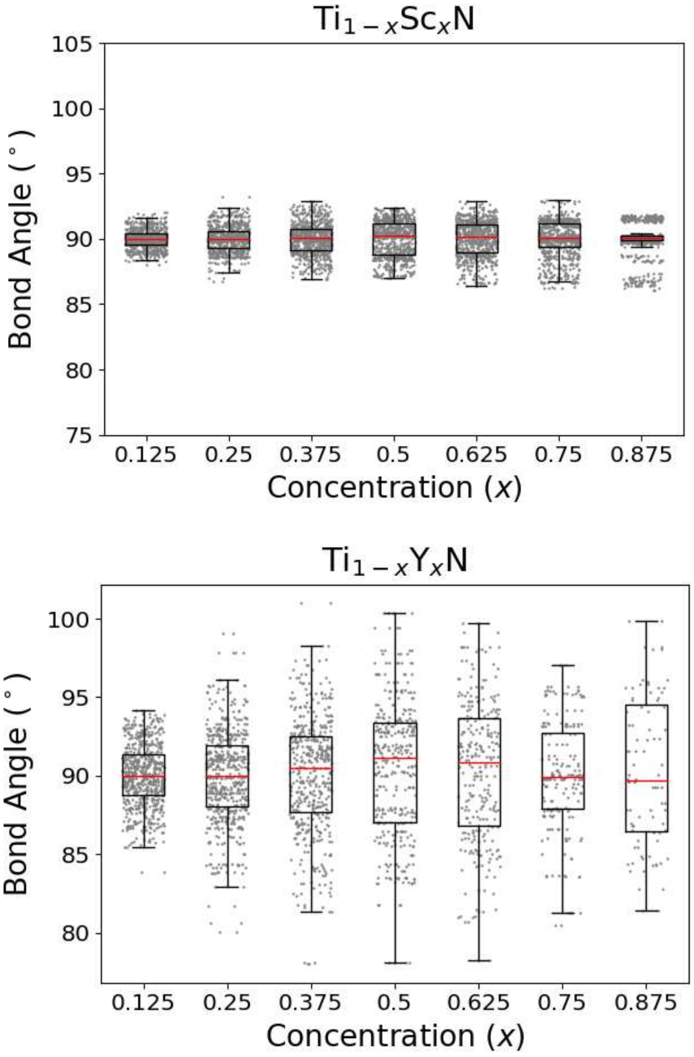

Figure 5. Distribution of the metal-nitrogen-metal bond angles (degrees) within the SQSs of $Ti_{1-x}Sc_xN$ (top) and $Ti_{1-x}Y_xN$ (bottom) as a function of Sc and Y concentration.

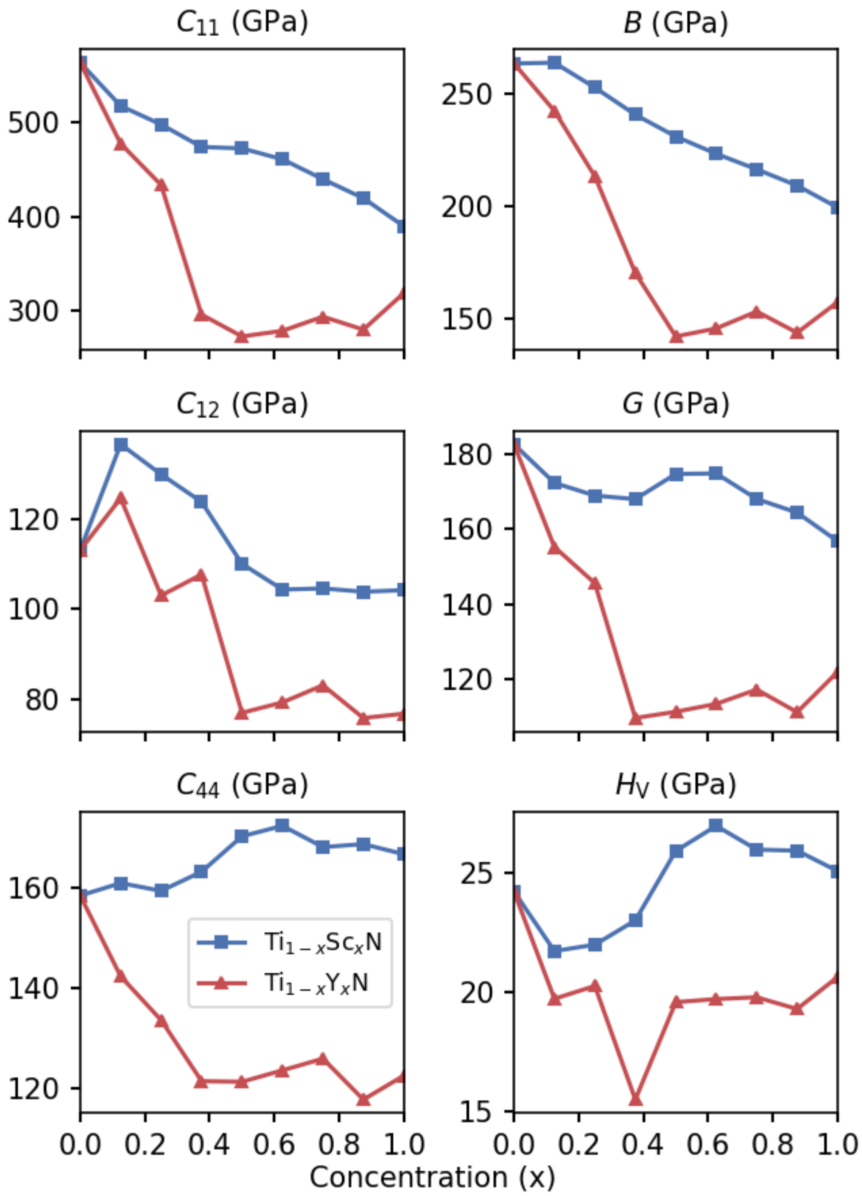

Figure 6. Elastic constants C_{11}, C_{12}, C_{44}, bulk moduli (B), shear moduli (G) and Vickers hardness (H_V) of the SQS's of $Ti_{1-x}Sc_xN$ and $Ti_{1-x}Y_xN$. Points represent explicitly calculated values, whereas lines are interpolations.

First principles investigation into the phase stability and enhanced hardness of TiN-ScN and TiN-YN alloys

V. Adhikari[1], N. J. Szymanski[1], I. Khatri[1], D. Gall[2], S. V. Khare[1*]

[1] *Department of Physics and Astronomy, The University of Toledo, 2801 West Bancroft Street, Toledo, OH 43606, USA*

[2] *Department of Materials Science and Engineering, Rensselaer Polytechnic Institute, 110 8th Street, Troy, NY 12180, USA*

*Corresponding author: sanjay.khare@utoledo.edu

SUPPLEMENTAL MATERIAL

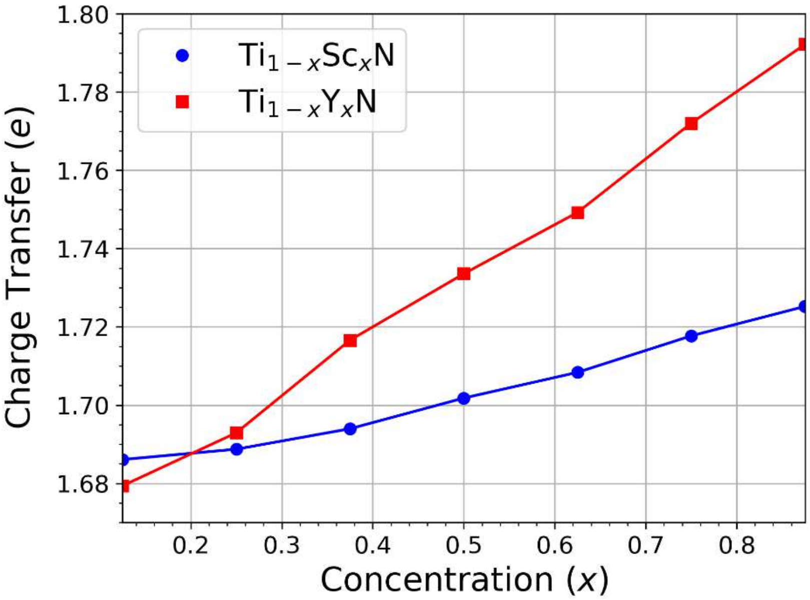

Figure S1. Bader charge transfer from metal (M) atoms to nitrogen (N) in the $Ti_{1-x}Sc_xN$ and $Ti_{1-x}Y_xN$ alloy system.

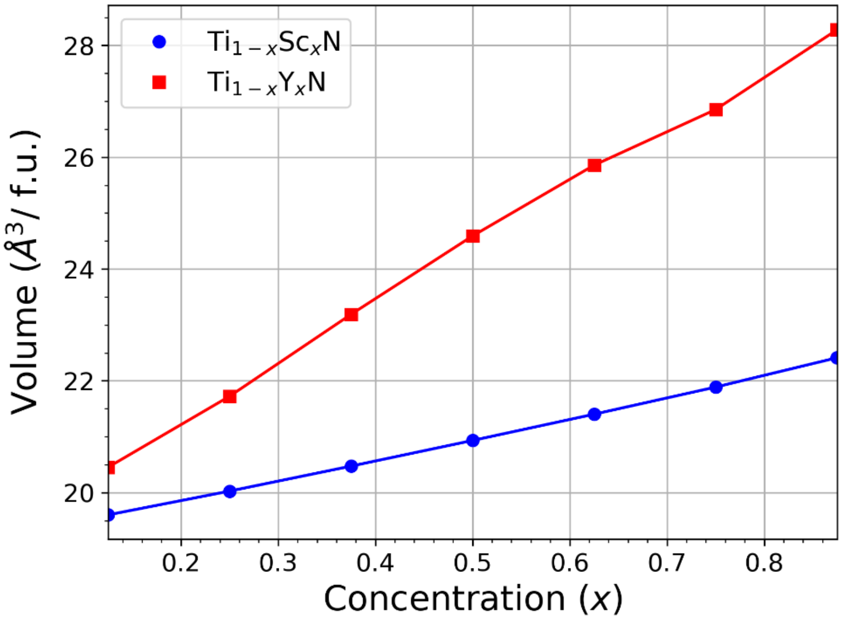

Figure S2. Variation in the unit cell volume per formula unit with the concentration (x) in the Ti$_{1-x}$Sc$_x$N and Ti$_{1-x}$Y$_x$N alloy system.

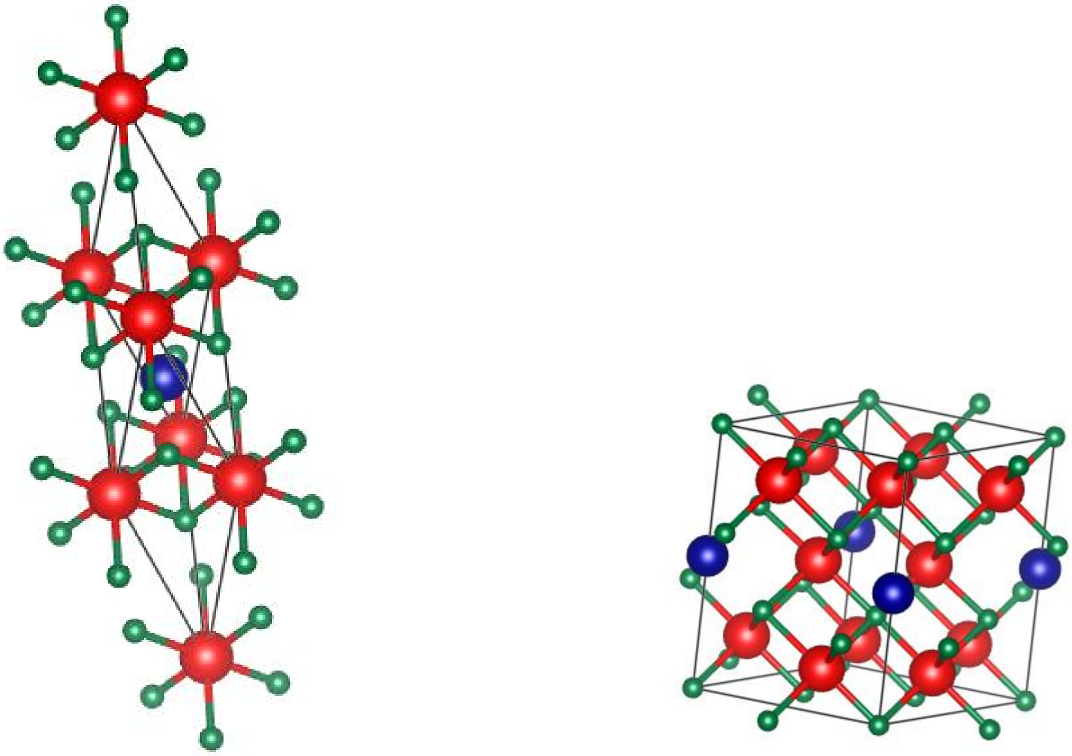

a) $TiScN_2$

b) $TiSc_8N_9$

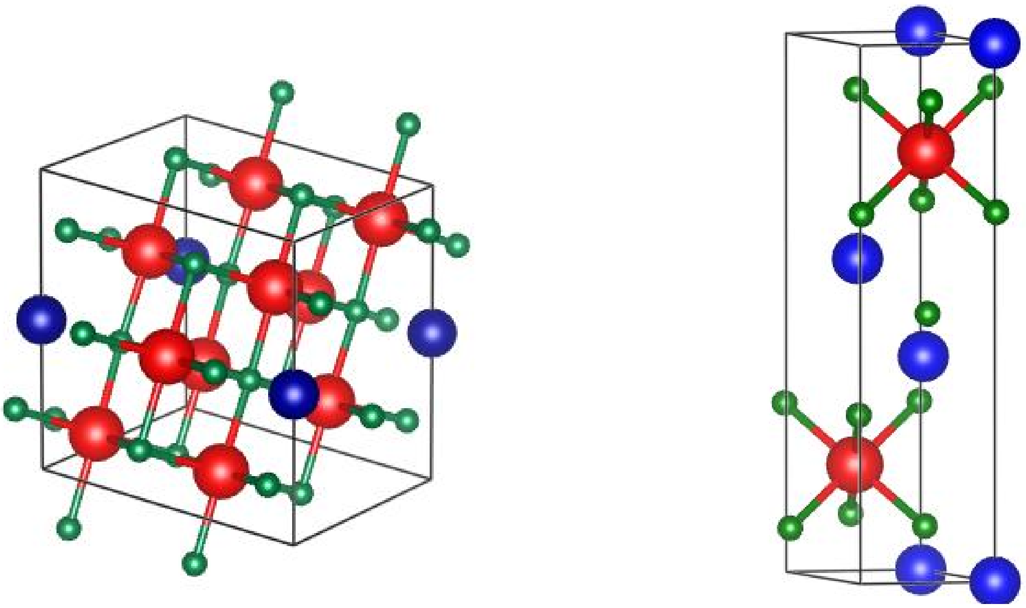

(c) $TiSc_9N_{10}$

(d) $Ti_3Sc_2N_5$

Figure S3: Computed Conventional unit cells of the predicted four novel ground states (a) $TiScN_2$, (b) $TiSc_8N_9$, (c) $TiSc_9N_{10}$ and (d) $Ti_3Sc_2N_5$. Blue, red and green spheres represent Ti, Sc and N atoms respectively.

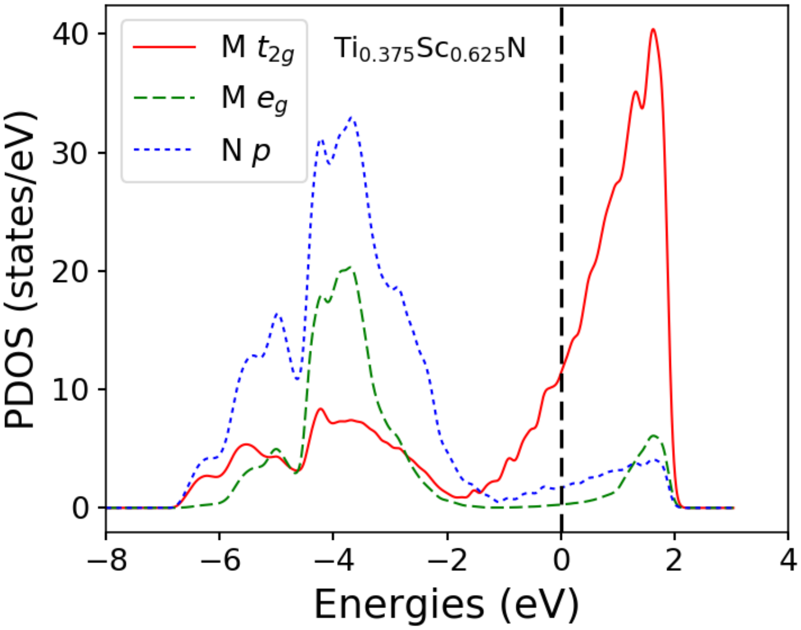

Figure S4. Projected density of states (PDOS) for the random solid solution $Ti_{0.375}Sc_{0.625}N$, which has the highest hardness. Red solid and green long-dashed lines represent the metallic t_{2g} an e_g states respectively while blue short-dashed lines indicate nitrogen p states.

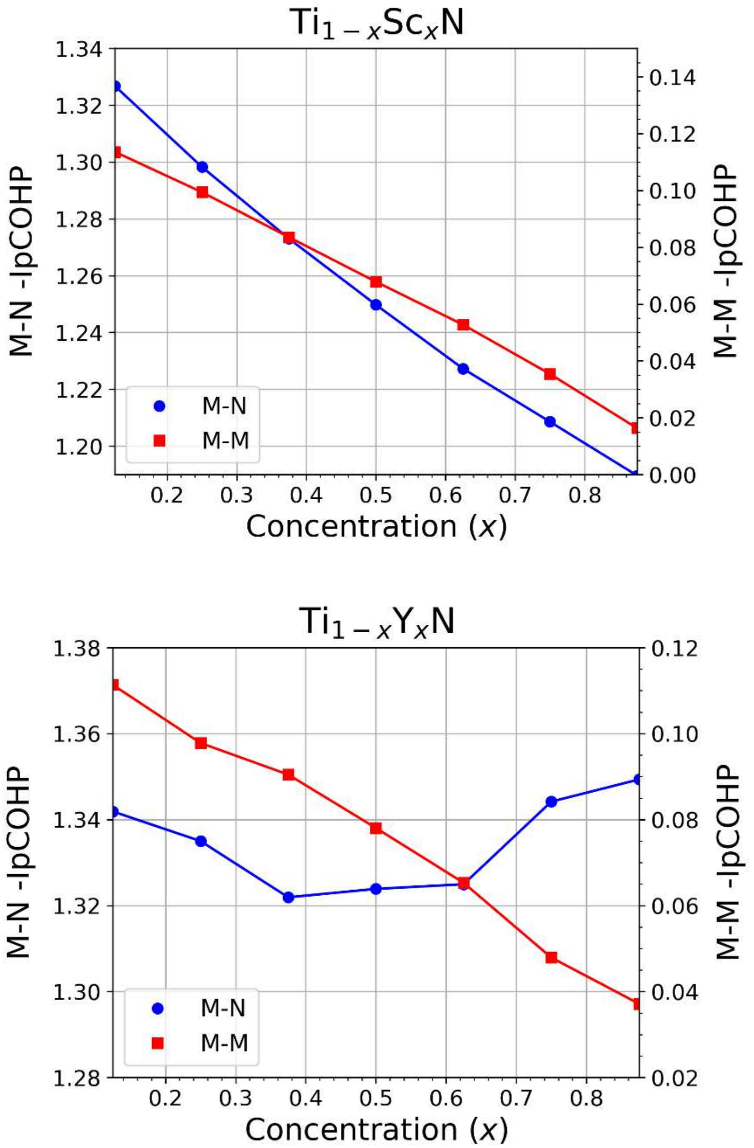

Figure S5. Integrated Crystal Orbital Hamilton Population (ipCOHP) for the SQS's of $Ti_{1-x}Sc_xN$ (top) and $Ti_{1-x}Y_xN$ (bottom) as a function of Sc and Y concentration.

Table S1. Numbers of structures calculated with DFT, numbers of clusters in pairs, triplets and quadruplets, and cross-validation (CV) score of $Ti_{1-x}Sc_xN$ and $Ti_{1-x}Y_xN$.

Alloys	Num. of structures	Num. of clusters (pair + trip + quad)	CV Score (meV)
$Ti_{1-x}Sc_xN$	83	15+2+3	4.04
$Ti_{1-x}Y_xN$	91	16+12+16	19.3

Table S2. The structural details (Lattice type, Hermann-Mauguin [1] notation for Space group - symbol and number, and Lattice parameters) of the four predicted novel ground states.

Predicted Ground States	Lattice - Type	Space Group and Number	Lattice Parameter
$TiScN_2$	Rhombohedral	$R\bar{3}m$ (166)	a = b = c = 5.35 Å, α = β = γ = 33.32°
$TiSc_8N_9$	Hexagonal	$P\bar{3}1m$ (162)	a = b = 5.46 Å, c = 7.72 Å, α = β = 90°, γ = 120°
$TiSc_9N_{10}$	Triclinic	$P\bar{1}$ (2)	a = 5.46 Å, b = 6.31 Å, c = 7.06 Å, α = 102.91°, β = 97.39°, γ=106.83°
$Ti_3Sc_2N_5$	Monoclinic	C2/m (12)	a = b = 3.07 Å, c = 12.69 Å, α = 90.00°, β = 83.02°, γ = 60.00°

Table S3. Integrated Crystal Orbital Hamilton Populations (IpCOHP) for different bonding states (Metal: Metal and Metal: Nitrogen) for the three end members and four predicted novel ground states.

Compound	M-N –IpCOHP	M-M -IpCOHP
TiN	1.415	0.137
ScN	1.428	0.012
YN	2.420	0.009
TiScN	1.408	0.043
$Ti_3Sc_2N_5$	1.721	0.078
$TiSc_8N_9$	1.255	-0.008
$TiSc_9N_{10}$	1.228	-0.009

Table S4. Concentration (*x*), elastic constants (C_{11}, C_{12}, C_{44}), Bulk modulus (*B*), Shear modulus (*G*), Pugh's ratio (*k*), Poisson's ratio (*v*), Young's modulus (*E*) and Vickers hardness (H_V) of the SQS of $Ti_{1-x}Y_xN$.

SQSs	Concentration (*x*)	C_{11} (GPa)	C_{12} (GPa)	C_{44} (GPa)	*B* (GPa)	*G* (GPa)	*k*	*v*	*E* (GPa)	H_V (GPa)
$Ti_{1x}Sc_xN$	0	563.2	113.1	158.6	263.1	182.5	0.69	0.22	444.7	24.2
	0.125	517.3	136.5	161.1	263.5	172.2	0.65	0.23	424.2	21.7
	0.25	497.6	129.9	159.5	252.4	168.8	0.67	0.23	414.2	22
	0.375	473.7	123.7	163.3	240.4	167.9	0.7	0.22	408.6	23
	0.5	472.2	110	170.4	230.7	174.6	0.76	0.2	418.3	25.9
	0.625	460.6	104.3	172.5	223.1	174.7	0.78	0.19	415.7	27
	0.75	439.5	104.6	168.2	216.2	167.9	0.78	0.19	400.2	26
	0.875	419.3	103.8	168.8	209	164.3	0.79	0.19	390.6	25.9
	1	389.5	104.2	166.8	199.3	156.7	0.79	0.19	372.5	25.1
$Ti_{1-x}Y_xN$	0	563.2	113.1	158.6	263.1	182.5	0.69	0.22	444.7	24.2
	0.125	477.2	124.6	142.5	242.1	155.2	0.64	0.24	383.5	19.7
	0.25	433.4	103	133.7	213.1	145.5	0.68	0.22	355.6	20.3
	0.375	295.7	107.7	121.6	170.3	109.7	0.64	0.23	270.9	15.5
	0.5	272.5	77	121.4	142.2	111.3	0.78	0.19	264.8	19.6
	0.625	278.5	79.3	123.7	145.7	113.4	0.78	0.19	270.2	19.7
	0.75	293.5	83.1	126	153.2	117.2	0.77	0.2	280.2	19.8
	0.875	279.7	75.8	117.9	143.8	111.2	0.77	0.19	265.3	19.3
	1	318.5	76.8	122.6	157.4	121.9	0.77	0.19	290.7	20.6

References:

[1] International Tables for Crystallography (2006), Vol. A (Editor: Theo Hahn, Published by Springer), Chapter 12.1.4 Hermann–Mauguin symbols, pp. 818–820.